



# Synthesis of mesoporous NiO nanospheres as anode materials for lithium ion batteries

Guanhua Zhang, Yuejiao Chen, Baihua Qu, Lingling Hu, Lin Mei, Danni Lei, Qing Li, Libao Chen, Qihong Li\*, Taihong Wang

Key Laboratory for Micro-Nano Optoelectronic Devices of Ministry of Education, and State Key Laboratory for Chemo/Biosensing and Chemometrics, Hunan University, Changsha 410082, China

## ARTICLE INFO

### Article history:

Received 16 April 2012  
Received in revised form 28 June 2012  
Accepted 29 June 2012  
Available online 6 July 2012

### Keywords:

Nickel oxide  
Nanospheres  
Lithium-ion batteries  
Anode material

## ABSTRACT

In this work, three-dimensional mesoporous NiO nanostructures have been synthesized by a simple ethylene glycol (EG)-mediated self-assembly route and subsequent calcination process. The synthesized nickel alkoxide precursors annealed at 300 and 500 °C exhibit different surface area, crystallinity and pore distribution, which have been characterized by scanning electron microscopy, transmission electron microscopy, selected area electron diffraction, X-ray diffraction, Fourier transform infrared spectroscopy and Nitrogen adsorption/desorption isotherms. The electrochemical properties of these NiO mesoporous nanostructures are investigated including the cycling and rate performance as anode materials for lithium-ion batteries. It is indicated that mesoporous NiO nanospheres synthesized at 500 °C exhibit better electrochemical performance than that obtained at 300 °C. The NiO nanospheres annealed at 500 °C present a reversible specific capacity of 518 mAh g<sup>-1</sup> at a current density of 0.1 A g<sup>-1</sup> after 60 cycles. With varying the rate from 0.1 to 8.0 A g<sup>-1</sup>, the capacity remains at 535 mAh g<sup>-1</sup> at 2 A g<sup>-1</sup> after 30 cycles and resumes to 582 mAh g<sup>-1</sup> at 0.1 A g<sup>-1</sup> after 60 cycles. The results indicate that our mesoporous NiO nanospheres are promising anode materials for lithium ion batteries.

© 2012 Elsevier Ltd. All rights reserved.

## 1. Introduction

Lithium ion batteries (LIBs), a fast-developing technology in electric energy storage, are the dominant power sources for a wide range of portable electronic devices [1–3]. Great efforts are underway to develop new electrode materials and new technologies for next generation LIBs. Recently, transition metal oxides (such as Co<sub>3</sub>O<sub>4</sub>, Fe<sub>3</sub>O<sub>4</sub> and NiO) have been extensively investigated as alternative anode materials for LIBs owing to high theoretical capacity (700–1000 mAh g<sup>-1</sup>) based on a novel conversion mechanism [4–8]. Among them, NiO has attracted considerable attention due to its high theoretical capacity (~718 mAh g<sup>-1</sup>), low cost, natural abundance and environmental friendliness. It has been shown that the electrochemical performance of NiO nanostructures largely depends on their morphology and surface properties [9–13]. Up to date, various NiO nanostructures have been used as anode materials including nanoparticles [14], nanotubes [15], hollow nanostructures [16,17], nanosheet assembled microspheres [18,19], and nanoflakes [20].

Three-dimensional (3D) porous nanostructures have been proved to be effective in improving their electrochemical

properties [21–23]. The improvement profits from their easy accessibility for the electrolyte (facilitating Li<sup>+</sup> ions transportation), which can accelerate phase transition and restrain the crumbling and cracking of the electrode, offering more connecting opportunities and positions with the electrode. In addition, the 3D porous structures with large surface-to-volume ratio and short diffusion length for lithium intercalation can lead to superior cycling and rate performance as electrode materials [23,24]. Thus the design and preparation of new electrode materials with 3D porous nanostructures will provide a tremendous opportunity to improve their electrochemical properties.

In this work, we report a simple and efficient approach to prepare nickel oxide precursors through an EG-mediated self-assembly process. Such a method has been adopted previously for the preparation of hollow NiO spheres [16], flowerlike CeO<sub>2</sub> [25], and SnO<sub>2</sub> nanowires [26]. However, in these previous studies, surfactants (such as polyvinylpyrrolidone) or other additives (for instance tetrabutylammonium bromide and urea) are necessary in the synthetic procedure; in this study we successfully synthesize nickel alkoxide without any use of surfactants, or additives. Furthermore, by calcinating at different temperatures, the as-obtained nickel alkoxide is transformed to 3D mesoporous structured NiO. The electrochemical properties of the NiO nanospheres are also investigated as anode materials for lithium ion battery. The initial discharge capacities of NiO annealed at 300 °C and 500 °C are

\* Corresponding author. Tel.: +86 731 88822137; fax: +86 731 88822137.  
E-mail address: [liqihong2004@hotmail.com](mailto:liqihong2004@hotmail.com) (Q. Li).

1026 and 1220 mAh g<sup>-1</sup> at a current density of 100 mA g<sup>-1</sup>, respectively. However, the NiO annealed at 300 °C exhibits a value of 222 mAh g<sup>-1</sup> after 60 cycles, while the NiO annealed at 500 °C shows better electrochemical performance of 518 mAh g<sup>-1</sup>. It indicates that the porous NiO nanospheres annealed at 500 °C have potential applications in lithium ion batteries.

## 2. Experimental

### 2.1. Synthesis

All chemical reagents utilized in the study were of analytical grade and used without further purification. In a typical preparation process, 5 mmol Ni(CH<sub>3</sub>COO)<sub>2</sub>·4H<sub>2</sub>O was dissolved in 100 mL ethylene glycol under stirring. After 30 min, the obtained green transparent solution was transferred into a 250-mL round flask and then refluxed at 170 °C for 10 h with constant magnetic stirring. After cooling to room temperature, the green precipitate was collected by centrifugation, washed with deionized water and absolute ethanol several times, and dried in an oven at 60 °C overnight. Finally, the products were annealed at 300 and 500 °C for 4 h, hereinafter designated as S-300 and S-500, respectively.

### 2.2. Characterization

The as-prepared products were characterized by a powder X-ray diffraction (XRD, Siemens D-5000) with Cu Kα (λ = 0.15418 nm). The morphology of the synthesized samples was examined using field-emission scanning electron microscopy (SEM, Hitachi S-4800) and transmission electron microscopy (TEM, JEOL-2010) operated at an accelerating voltage of 200 kV. Specific surface area and porosity analysis for the samples were performed through measuring Brunauer–Emmett–Teller (BET) nitrogen adsorption–desorption isotherms with a Micromeritics ASAP2020 apparatus. Fourier transform infrared (FT-IR) spectra were recorded for a KBr diluted sample using a Bruker Vertex 70 spectrometer with a resolution of 4 cm<sup>-1</sup>.

### 2.3. Electrochemical measurements

A CR2025-type coin cell was assembled to investigate the electrochemical properties of the products. The working electrodes were prepared by mixing 80 wt% active material, 10 wt% acetylene black (Super-P), and 10 wt% binder (LA133 and CMC) in distilled water and absolute alcohol mixture. After coating the above slurries

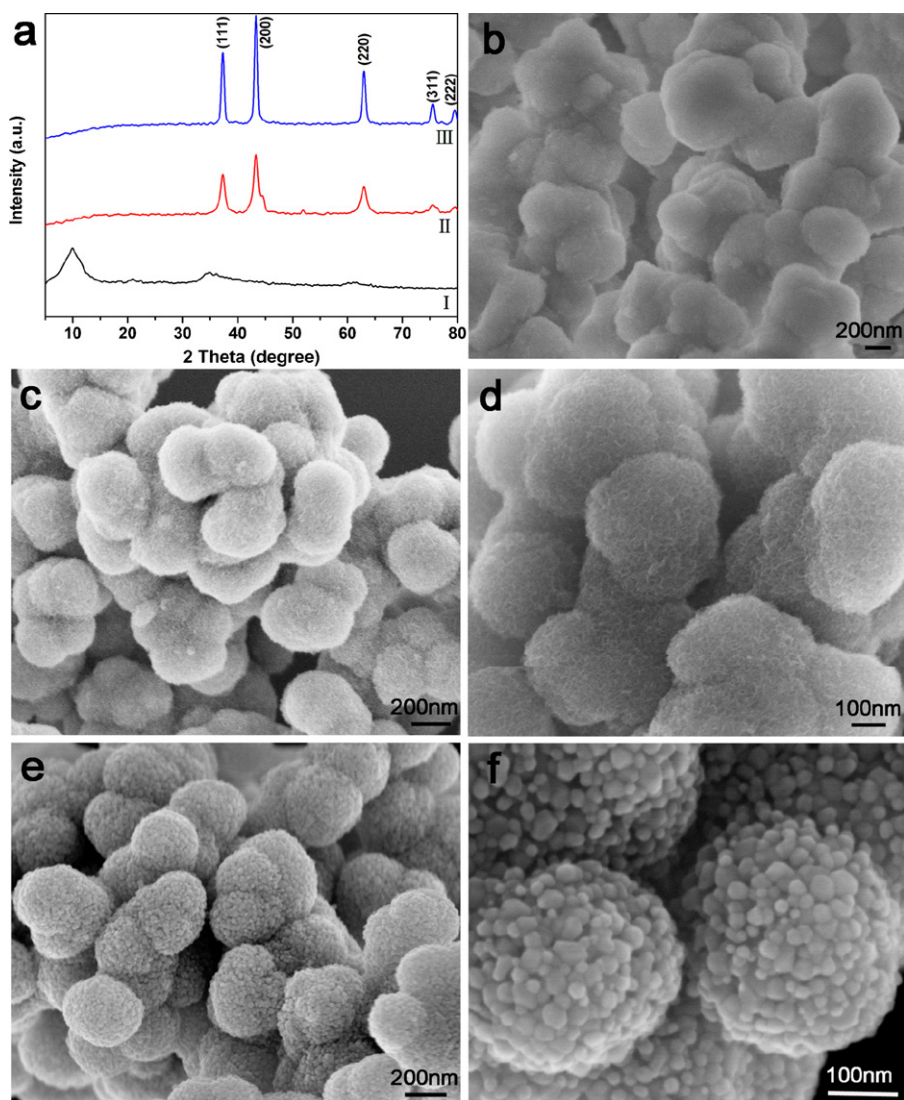


**Fig. 1.** (a) XRD patterns of (I) as-synthesized NiO precursor, (II) S-300, (III) S-500; (b) SEM image of as-synthesized NiO precursors; (c, d) SEM image and magnified SEM image of S-300, respectively; (e, f) SEM image and magnified SEM image of S-500, respectively.

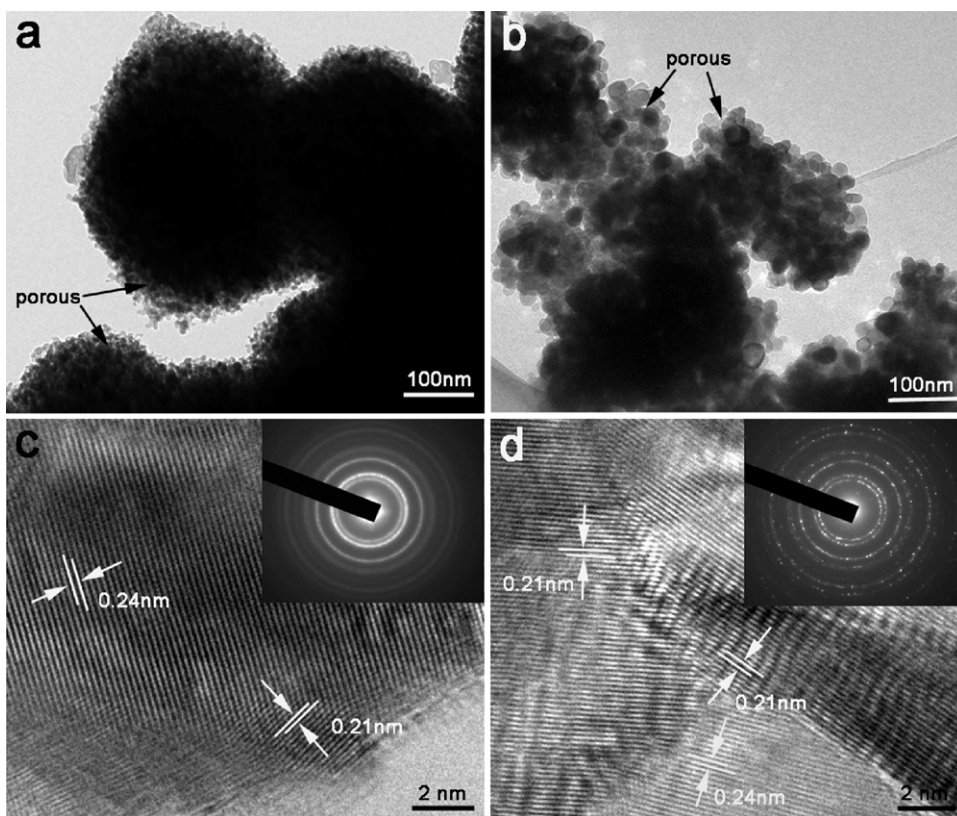


**Fig. 2.** (a, b) TEM images of S-300 and S-500, respectively; (c, d) HR-TEM images of S-300 and S-500, with corresponding SAED patterns (inset), respectively.

on a copper foil, the electrodes were dried at 80 °C under vacuum to remove the solvent. The cells were assembled in an argon-filled glovebox with water and oxygen contents less than 1 ppm. A Celgard 2400 microporous polypropylene membrane was used as a separator. The electrolyte consisted of a solution of 1 M LiPF<sub>6</sub> in ethylene carbonate/dimethyl carbonate/diethyl carbonate (1:1:1, in weight percent). Pure lithium foil was used as a counter electrode. The discharge and charge measurements were carried out on an Arbin BT2000 system with the cut off potentials being 0 and 3 V at different current densities from 0.1 to 8.0 A g<sup>-1</sup>. The CV experiment was also tested on the Arbin battery test system at a scan rate of 0.5 mV s<sup>-1</sup>.

### 3. Results and discussion

Fig. 1a shows the X-ray diffraction (XRD) patterns of the as-obtained nickel oxide precursor and the thermally decomposed products at 300 and 500 °C. The XRD pattern of the nickel alkoxide shows a strong low-angle reflection with characteristically strong peaks at around 10°. Such XRD features are also found on several other EG-mediated metal glycolates. It was considered to be a typical feature from the coordination and alcoholysis of EG with the center metal ions [25–28]. The XRD pattern of the calcined product matches well with the single phase of face-centered cubic NiO (JCPDS No. 47-1049). Furthermore, with increasing the calcination temperature, the intensities of the diffraction peaks become intense and sharp, which indicates that NiO nanoparticles obtained at a higher calcination temperature are better crystallized with larger crystallite sizes. Fig. 1b shows the typical SEM image of the nickel oxide precursor. It is composed of many irregular spheres with a diameter of 200–500 nm. The surface of the nanospheres is smooth and no isolated nanoparticles can be detected. When the precursor was calcined at 300 °C, the morphology of S-300 can maintain

a basic shape of the precursor but the surface of the nanospheres became rough, as shown in Fig. 1c. The high magnification SEM image (Fig. 1d) reveals large quantities of grains which are agglomerated loosely on the surface of nanospheres. The morphology of S-500 is displayed in Fig. 1e, which also exhibits basic shape of the precursor but the size of spheres decreases. The nanospheres are porous and constructed by aggregation of a lot of nanoparticles with an average size about 20 nm as shown by the high magnification SEM image (Fig. 1f).

The detailed morphological and structural features of the powders are also examined by TEM. Fig. 2a shows the TEM image of S-300. It can be seen that the nanosphere consists of nanocrystals with diameters of 5–10 nm, which arrange randomly and connect with each other. Many pores can be detected at the edge of the nanosphere. Fig. 2b shows the TEM image of S-500, the diameters of the nanocrystals along with the nanopores grow larger, because of the fusion between the nanocrystals at a higher annealing temperature. In addition, the high resolution TEM (HR-TEM) image (Fig. 2c and d) of an individual NiO nanosphere indicates that there are two types of lattice fringes with lattice of 0.24 and 0.21 nm, corresponding to the (1 1 1) and (2 0 0) crystalline plane of face-centered cubic NiO. The selected area electron diffraction (SAED) pattern (the inset of Fig. 2c and d) shows several Debye–Scherrer rings, corresponding to the reflections of the NiO polycrystals.

For further investigation of the chemical composition of the as-prepared NiO precursor, the FT-IR measurement was carried out. Fig. 3 shows the IR spectroscopic spectrum of the precursor. The vibrational bands of CH<sub>2</sub> in the range of 2850–2950 cm<sup>-1</sup> as well as the stretching band of C–O at 1061 cm<sup>-1</sup> derived from the ethylene glycol unit are observed. Simultaneously, the strong absorption bands of C=O in acetate ions at 1590 cm<sup>-1</sup> are also detected. Thus, it can be concluded that the as-synthesized nickel oxide precursor is probably a kind of nickel alkoxide and that the structure might be similar to those of nickel alkoxide and cerium alkoxide [16,25].

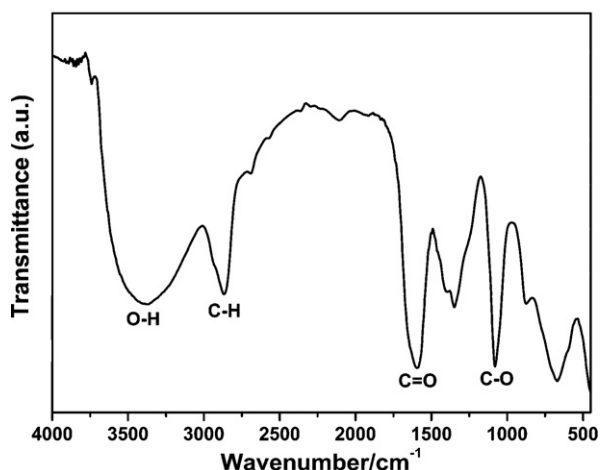
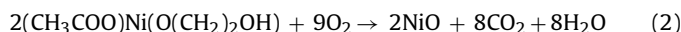
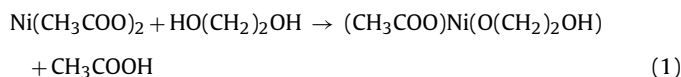


Fig. 3. FT-IR spectra of as-synthesized NiO precursor.

Based on the above results, we elucidate a plausible mechanism responsible for the formation of NiO nanospheres (Fig. 4). During the synthesis process, EG first coordinated with  $\text{Ni}(\text{CH}_3\text{COO})_2$  to produce nickel alkoxide, which precipitated to become the nuclei [16,29]. In the following secondary growth stage, the nickel alkoxide underwent several steps of intermediate reactions and eventually led to the formation of longer chains, which could further self-assemble into nanospheres through van der Waals interactions and hydrogen bonds [25,29]. Ultimately, the obtained NiO precursor was thermally decomposed to NiO through annealing in air. Such a process is consistent with previous reports of a so-called two-stage growth followed by a slow aggregation and crystallization of primary particles [16,25,29–33]. Further work is underway to investigate the detail of the self-assembly growth mechanism. According to the previous papers [16,25,33], the related reaction equations can be described as follows:



The role of acetate was found to be very critical in this synthesis method. In a control experiment, when nickel acetate was replaced by nickel sulfate under the same reaction conditions, no apparent precipitate was obtained. In our experiment, when EG served as a ligand and coordinated with  $\text{Ni}^{2+}$  to form nickel alkoxide, it would be associated with producing acid ( $\text{H}_2\text{SO}_4$  or  $\text{CH}_3\text{COOH}$ ). Sulfuric acid is a vigorous proton acid, the accumulation of  $\text{H}^+$  would inhibit further nickel alkoxide formation with the elongated time. Nevertheless, acetic acid is more difficult to ionize, thus allowing the coordination reaction to be completed.

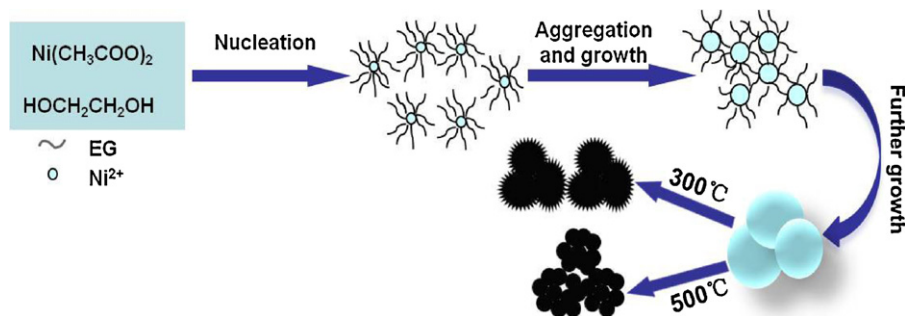


Fig. 4. Schematic illustration of the preparation of the NiO nanospheres.

The textural properties of the NiO samples were further investigated by nitrogen sorption and desorption isotherms and corresponding pore size distribution (inset) are shown in Fig. 5. It can be seen that the specific surface areas are calculated using the BET method and are determined to be  $80.5$  and  $15.8 \text{ m}^2 \text{ g}^{-1}$  for S-300 and S-500, respectively. When it comes to the temperature of  $300^\circ\text{C}$ , the pore size distribution reveals with mean diameter of  $26 \text{ nm}$  (Fig. 5a, inset). With the annealing temperature increasing to  $500^\circ\text{C}$ , crystallites grow larger via thermal re-crystallization. Meanwhile, some small mesopores gradually heal and diminish, but some other mesopores may gradually merge and become bigger. As a result, the inter-crystallite pores become larger, the pore size distribution reveals a bimodal nature with mean diameters of  $32$  and  $48 \text{ nm}$  (Fig. 5b, inset). The porous structure cannot only benefit the diffusion of solid-state Li-ion [34–38], but also accommodate volume changes of charge/discharge process to maintain the structure integrity [39,40].

In order to investigate the lithium storage properties, the NiO was used as positive electrode with a standard NiO/Li half-cell configuration. Fig. 6 shows the charge–discharge curves for the 1st, 2nd, 10th, 30th and 60th cycle. The corresponding discharge capacities of S-300 are  $1026$ ,  $848$ ,  $611$ ,  $346$ ,  $222 \text{ mAh g}^{-1}$ , respectively. Those discharge capacities of S-500 are up to  $1220$ ,  $866$ ,  $772$ ,  $586$ ,  $518 \text{ mAh g}^{-1}$ , respectively. In general, these charge–discharge curves present similar profiles. The initial discharge shows a clear potential plateau at  $\sim 0.6$  vs.  $(\text{Li}/\text{Li}^+)/\text{V}$  followed by a sloping curve, which corresponds to the following convention reaction:



The sloping part in the end of the discharge curve between  $0.6$  and  $0 \text{ V}$  corresponds to the formation of the solid electrolyte interface (SEI) layer [41,42]. The charge and discharge plateaus are not obvious since the second cycle. There are two slopes around  $1.6$  and  $2.3 \text{ V}$  in each charge curve, and the slop in each discharge curve is around  $1.3 \text{ V}$ . According to Fig. 6, it is apparent that the charge/discharge performance and cycleability of S-500 are better than S-300. In addition, the discharge capacity of S-500 after 60 cycles is  $518 \text{ mAh g}^{-1}$ , which is about 1.5 times that of current carbon-based electrode materials. This improved cycling performance might be attributed to the robust mesoporous structure and improved crystallinity [43–45]. The initial discharge capacities of S-500 and S-300 are  $1220$  and  $1026 \text{ mAh g}^{-1}$ . Both of them are significantly higher than the theoretical capacity. The extra capacities are mainly due to the decomposition of non-aqueous electrolyte during the discharge process [46].

The lithium storage capacities of porous NiO nanospheres were determined by galvanostatic charge/discharge cycling at the current density of  $100 \text{ mA g}^{-1}$ . As shown in Fig. 7, the capacity of S-300 decreases sharply as the cycle number increases. It can be seen that the discharge capacity of S-500 is maintained at  $\sim 447 \text{ mAh g}^{-1}$  after 80 cycles, while S-300 exhibits a value of  $\sim 148 \text{ mAh g}^{-1}$ . Poizot

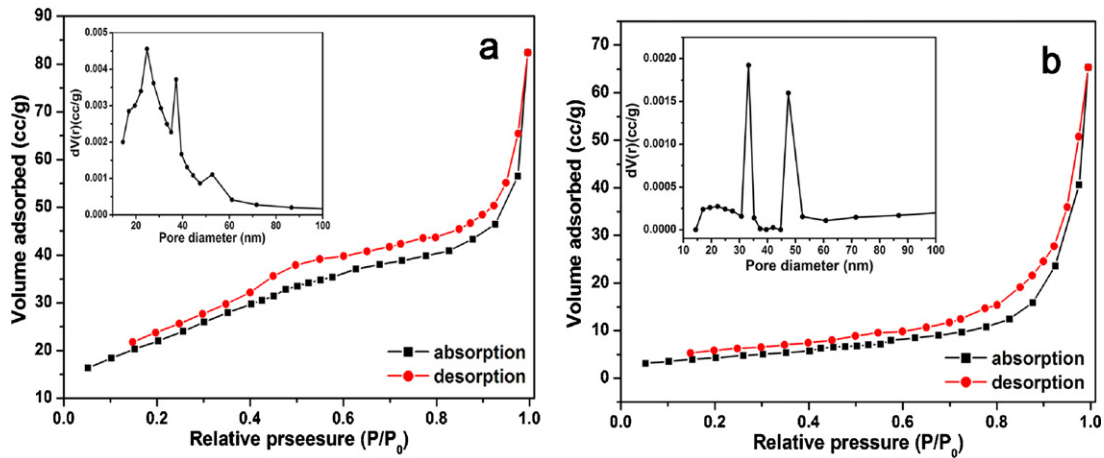


Fig. 5.  $N_2$  adsorption/desorption isotherm curve of NiO nanospheres and Barrett–Joyner–Halenda (BJH) pore size distribution plot (inset): (a) S-300 and (b) S-500.

et al. suggest that for each metal oxide system there is an optimum particle size and hence the best electrochemical performance [8,9]. It can be inferred that several factors (surface area, grain size, crystallinity and structure stability) are competing with each other, which may affect the Li-ion storage performance [43,47,48]. In the previous reports, Zhu et al. summarized that the optimal grain size, crystallinity and morphology codetermined the anode material's property [47]. Yan et al. also reached a similar conclusion and further pointed out that well-crystalline material could maintain the nanosize crystallite and activate the decomposition of  $Li_2O$ , thus

increasing the discharge capacity [43]. For samples annealed at a low temperature, their specific surface area is high but their crystallinity is poor. In this case, the diffusion of the Li in the grain is not efficient. Therefore, the electrochemical enhancement of S-500 might be attributed to its appropriate grain size and robust porous structure with improved crystallinity. In order to further explain the electrochemical processes, the materials after 20 cycles have been characterized by SEM. Fig. 8a and b shows the SEM images of the resultant materials after cycling, respectively. By comparing SEM images before and after cycling of the electrode, the spherical structure maintains basically after cycling. Nevertheless, the agglomeration and volume expansion of S-300 are more obvious, which might be attributed to the reason that the grain size and pore structure changed significantly during repeated charge/discharge processes. To further understand the detailed influences of these factors on the electrochemical performance, more in-depth investigations are still underway.

Compared with the reported performances of nanotube [49], net structure [50], flower-like microspheres [18], nanosheet-based microspheres [51], and spheres [52], the cyclic stability of our sample synthesized at  $500^\circ\text{C}$  is much enhanced, as shown in Table 1. As we all know, the diffusion length for lithium ion and electron is especially important for cycling. What is more, the 3D porous structures with large surface-to-volume ratio and short diffusion length for lithium intercalation can lead to superior cycling and rate performance of electrode materials [23,24]. For our structure, the porous structure provides space for volume expansion during

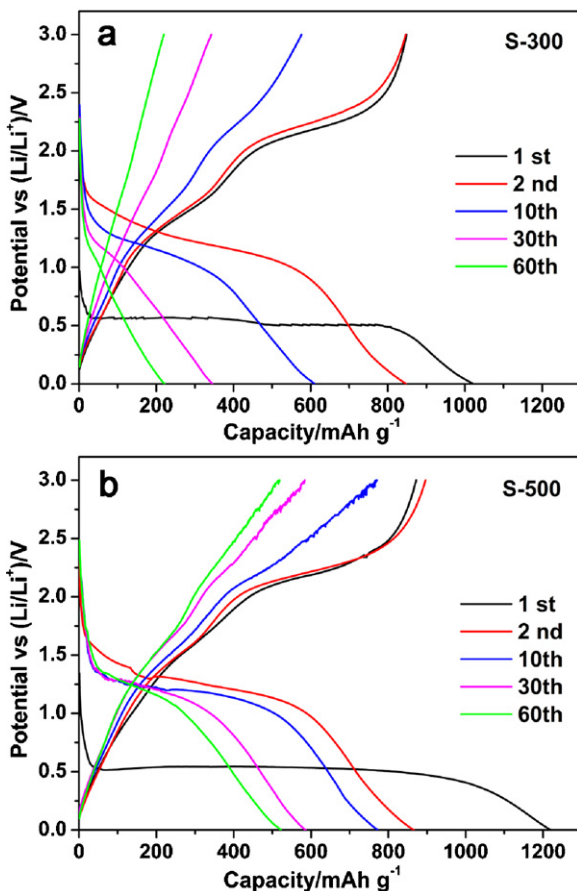


Fig. 6. Galvanostatic lithium-insertion/extraction curves of NiO electrodes between 0 and 3.0 V at a current density of  $100\text{ mA g}^{-1}$ : (a) S-300 and (b) S-500.

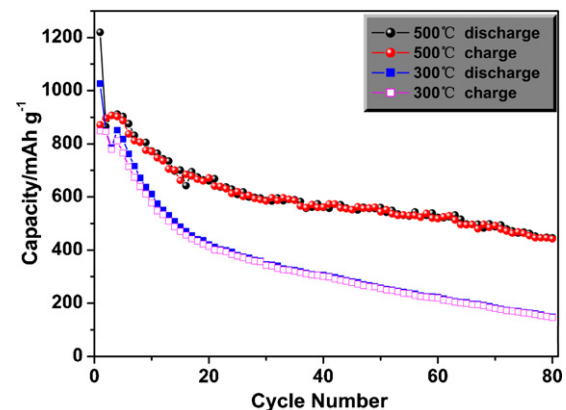


Fig. 7. Charge/discharge capacities vs. cycle number of NiO nanospheres at the same current density of  $100\text{ mA g}^{-1}$  between 0 and 3.0 V.

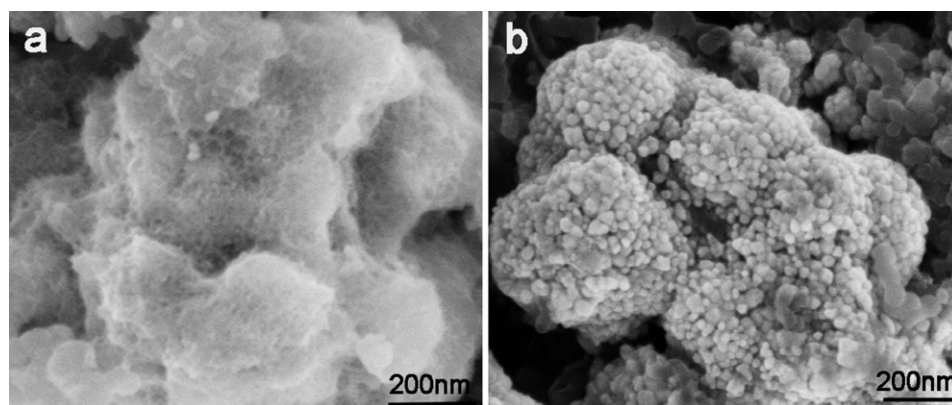


Fig. 8. SEM images of the electrodes after 20 cycles between 0 and 3.0 V at a current density of  $100 \text{ mA g}^{-1}$ : (a) S-300 and (b) S-500.

lithiation. Moreover, these grains enlarge and adhere together to form a compact layer, which have high stability and preserve the integrity of the structure. Therefore, we propose that high stability of the mesoporous structure is responsible for the improved performances.

Fig. 9 shows the representative discharge/charge voltage profiles of the electrodes with the current densities ranging from  $100 \text{ mA g}^{-1}$  ( $0.14 \text{ C}$ ,  $1 \text{ C} = 718 \text{ mA g}^{-1}$ ) to  $8000 \text{ mA g}^{-1}$  ( $11.2 \text{ C}$ ). With increasing the discharge/charge rate, the discharge potential decreases and the charge potential increases due to kinetic effects of the material, rendering higher overpotential [53]. The rate capability of the two samples was demonstrated in Fig. 10. They have the similar decreasing trends for the capacity along with the increasing current rates. However, the capacity of cells with S-300 NiO anode dropped more rapidly than that of S-500 NiO anode. The capacity difference between these two samples is reduced at the high current density ( $8000 \text{ mA g}^{-1}$ ), which can be ascribed to the structure collapse at higher current rates, making the gap between them minish. When the current rate resumes to  $0.14 \text{ C}$ , it is impressive to observe a specific storage capacity of  $582 \text{ mAh g}^{-1}$  for S-500 after 60-cycle discharge, while only  $310 \text{ mAh g}^{-1}$  is obtained for S-300. The stark contrast between the two samples demonstrates that mesoporous NiO spheres assembled by nanoparticles with better crystallinity are suitable for electrodes of LIBs. As compared to NiO net-structure and NiO hollow microspheres [15,50], the porous NiO nanospheres exhibit better rate capability. Such considerable improvement is believed to be caused by the high stability of the unique 3D porous structure and shorter  $\text{Li}^+$  diffusion length.

The cyclic voltammetric (CV) curves of S-500 were tested over a potential range from 0 to 3.0 V at a scan rate of  $0.5 \text{ mV s}^{-1}$ . As shown in Fig. 11, in the first cathodic scan, a large cathodic peak starts at 0.22 V corresponding to the initial reduction of  $\text{Ni}^{2+}\text{O}$  to metallic Ni, accompanying the formation of  $\text{Li}_2\text{O}$ . During the first anodic scan, two oxidation peaks are found at 1.63 and 2.26 V. The weak peak at 1.63 V should correspond to the dissolution of the organic SEI layer [53,54], and the strong peak at 2.26 V corresponds to the

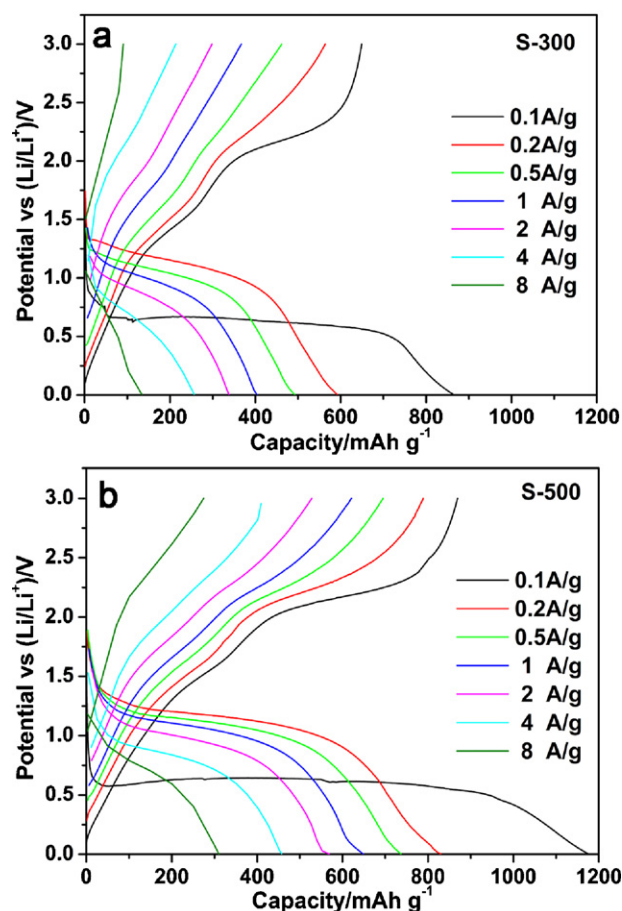


Fig. 9. Representative discharge/charge voltage profiles of (a) S-300 and (b) S-500 at various current densities.

Table 1

Comparison of the electrochemical properties of NiO synthesized at  $500^\circ\text{C}$  in this work with those of NiO reported in the literature.

Sample	Current density ( $\text{mA g}^{-1}$ )	Potential range (V vs. $\text{Li/Li}^+$ )	Initial capacity ( $\text{mAh g}^{-1}$ )	Capacity retention ( $\text{mAh g}^{-1}$ )	Ref.
NiO nanosphere	100	0.0–3.0	1220	518 after 60 cycles	This work
NiO nanotube	25	0.01–3.0	~610	200 after 20 cycles	[49]
Net-structured NiO	71.8	0.02–3.0	1190	178 after 40 cycles	[50]
Flower-like NiO	50	0.01–3.0	1276	219 after 40 cycles	[18]
Nanosheet-based NiO	50	0.01–3.0	1570	100 after 30 cycles	[51]
Spherical NiO	100	0.01–3.0	1147	367 after 50 cycles	[52]

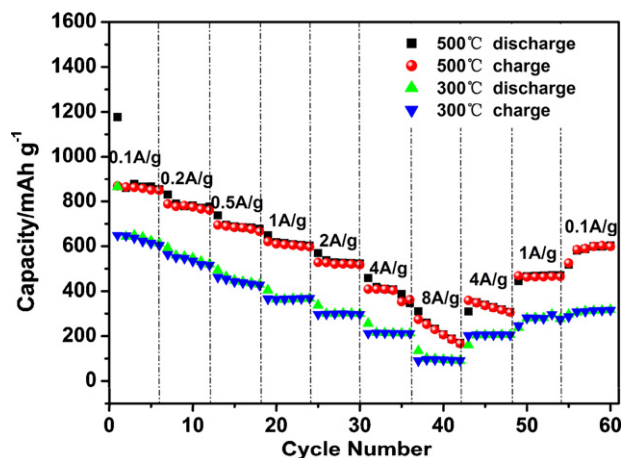


Fig. 10. Rate performances of the NiO nanospheres between 0 and 3.0 V at various current densities.

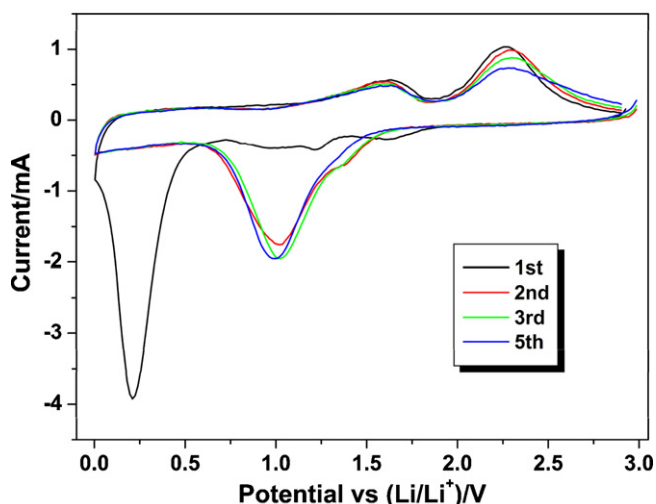


Fig. 11. The cyclic voltammogram (CV) curves of S-500 electrodes at a scan rate of  $0.5 \text{ mV s}^{-1}$  over a potential range from 0 to 3.0 V.

NiO formation, accompanying the decomposition of  $\text{Li}_2\text{O}$  [53,55]. During the anodic process, both the peak current and the integrated area of the anodic peak are decreased, indicating capacity loss during the charging process. In the subsequent 2nd and 3rd cycles, the cathodic peak potentials shift to 1.02 and 1.03 V, respectively. After the electrode activation during five cycles, the stable electrochemical process has been set up.

#### 4. Conclusions

We have developed a facile approach to produce porous NiO nanospheres. The grain size and surface area of as-synthesized porous NiO nanospheres can be tuned using the annealing temperature. The as-synthesized porous NiO nanospheres have been applied as the anode of LIBs. Compared with the S-300 nanospheres, the S-500 electrode exhibits superior cycling performance and higher rate capability. It can deliver a high reversible capacity up to  $\sim 447 \text{ mAh g}^{-1}$  after 80 cycles at a current density of  $100 \text{ mA g}^{-1}$ , and a capacity up to  $582 \text{ mAh g}^{-1}$  in the 60th cycle after cycling with various current densities from 100 to  $8000 \text{ mA g}^{-1}$ . Even at a current density as high as  $8000 \text{ mA g}^{-1}$ , the electrode can deliver a capacity higher than  $228 \text{ mAh g}^{-1}$ . The electrochemical enhancement of S-500 could be mainly ascribed to its appropriate grain size and the robust porous structure with improved crystallinity.

Furthermore, it is also noteworthy that this work may provide a simple and efficient approach for the large-scale synthesis of other 3D complex metal oxide nanomaterials.

#### Acknowledgements

We gratefully acknowledge financial support from the National Natural Science Foundation of China (Grant Nos. 21003041, 21103046), and Hunan Provincial Natural Science Foundation of China (Grant Nos. 11FH003, 10JJ1011).

#### References

- [1] M. Armand, J.M. Tarascon, *Nature* 451 (2008) 652.
- [2] X.L. Sun, X.H. Wang, L. Qiao, D.K. Hu, N. Feng, X.W. Li, Y.Q. Liu, D.Y. He, *Electrochimica Acta* 66 (2012) 204.
- [3] J.S. Chen, L.A. Archer, X.W. Lou, *Journal of Materials Chemistry* 21 (2011) 9912.
- [4] P. Poizot, S. Laruelle, S. Grugeon, L. Dupont, J.M. Tarascon, *Nature* 407 (2000) 496.
- [5] P.G. Bruce, B. Scrosati, J.M. Tarascon, *Angewandte Chemie International Edition* 47 (2008) 2930.
- [6] Y. Li, B. Tan, Y. Wu, *Nano Letters* 8 (2008) 265.
- [7] C.C. Li, X.M. Yin, Q.H. Li, L.B. Chen, T.H. Wang, *Chemistry – A European Journal* 17 (2011) 1596.
- [8] W. Xing, F. Li, Z.F. Yan, G.Q. Lu, *Journal of Power Sources* 134 (2004) 324.
- [9] C.Y. Cao, W. Guo, Z.M. Cui, W.G. Song, W. Cai, *Journal of Materials Chemistry* 21 (2011) 3204.
- [10] F. Jiao, A.H. Hill, A. Harrison, A. Berko, A.V. Chadwick, P.G. Bruce, *Journal of the American Chemical Society* 130 (2008) 5262.
- [11] T.Y. Wei, C.H. Chen, H.C. Chien, S.Y. Lu, C.C. Hu, *Advanced Materials* 22 (2010) 347.
- [12] C.Z. Yuan, X.H. Zhang, L.H. Su, B. Gao, L.F. Shen, *Journal of Materials Chemistry* 19 (2009) 5772.
- [13] J.W. Lang, L.B. Kong, W.J. Wu, Y.C. Luo, L. Kang, *Chemical Communications* 35 (2008) 4213.
- [14] S. Needham, G. Wang, H. Liu, *Journal of Power Sources* 159 (2006) 254.
- [15] X.H. Huang, J.P. Tu, C.Q. Zhang, F. Zhou, *Electrochimica Acta* 55 (2010) 8981.
- [16] X. Song, L. Gao, *Journal of Physical Chemistry C* 112 (2008) 15299.
- [17] L. Liu, Y. Li, S. Yuan, M. Ge, M. Ren, C. Sun, Z. Zhou, *Journal of Physical Chemistry C* 114 (2010) 251.
- [18] J.M. Ma, J.Q. Yang, L.F. Jiao, Y.H. Mao, T.H. Wang, X.C. Duan, J.B. Lian, W.J. Zheng, *CrystEngComm* 14 (2012) 453.
- [19] S.B. Ni, T. Li, X.L. Yang, *Materials Chemistry and Physics* 132 (2012) 1108.
- [20] Y. Li, B. Tan, Y. Wu, *Nano Letters* 8 (2008) 265.
- [21] M.H. Park, K. Kim, J. Kim, J. Cho, *Advanced Materials* 22 (2010) 415.
- [22] J. Wang, G. Du, R. Zeng, B. Niu, Z. Chen, Z. Guo, S. Dou, *Electrochimica Acta* 55 (2010) 4805.
- [23] B.H. Qu, M. Zhang, D.L. Lei, Y.P. Zeng, Y.J. Chen, L.B. Chen, Q.H. Li, Y.G. Wang, T.H. Wang, *Nanoscale* 3 (2011) 3646.
- [24] J.T. Zai, X.F. Qian, K.X. Wang, C. Yu, L.Q. Tao, Y.L. Xiao, J.S. Chen, *CrystEngComm* 14 (2012) 1364.
- [25] L.S. Zhong, J.S. Hu, A.M. Cao, Q. Liu, W.G. Song, L.J. Wan, *Chemistry of Materials* 19 (2007) 1648.
- [26] Y.L. Wang, X.C. Jiang, Y.N. Xia, *Journal of the American Chemical Society* 125 (2003) 16176.
- [27] X.C. Jiang, Y.L. Wang, T. Herricks, Y.N. Xia, *Journal of Materials Chemistry* 14 (2004) 695.
- [28] S. Laruelle, S. Grugeon, P. Poizot, M. Dollé, L. Dupont, J.M. Tarascon, *Journal of the Electrochemical Society* 149 (2002) A627.
- [29] Q.Q. Xiong, J.P. Tu, Y. Lu, J. Chen, Y.X. Yu, Y.Q. Qiao, X.L. Wang, C.D. Gu, *Journal of Physical Chemistry C* 116 (2012) 6495.
- [30] Y. Cheng, Y.S. Wang, Y.H. Zheng, Y. Qin, *Journal of Physical Chemistry B* 109 (2005) 11548.
- [31] R.L. Penn, *Journal of Physical Chemistry B* 108 (2004) 12707.
- [32] J. Park, V. Privman, E. Matijevic, *Journal of Physical Chemistry B* 105 (2001) 11630.
- [33] L.S. Zhong, J.S. Hu, H.P. Liang, A.M. Cao, W.G. Song, L.J. Wan, *Advanced Materials* 18 (2006) 2426.
- [34] B.Q. Liu, Q.F. Li, B. Zhang, Y.L. Cui, H.F. Chen, G.N. Chen, D.P. Tang, *Nanoscale* 3 (2011) 2220.
- [35] D.W. Liu, B.B. Garcia, Q.F. Zhang, Q. Guo, Y.H. Zhang, S. Sepelri, G.Z. Cao, *Advanced Functional Materials* 19 (2009) 1015.
- [36] C.M. Park, J.K. Jeon, *Chemical Communications* 47 (2011) 2122.
- [37] X.W. Lou, D. Deng, J.Y. Lee, L.A. Archer, *Chemistry of Materials* 20 (2008) 6562.
- [38] H.S. Zhou, D.L. Li, M. Hibino, I. Honma, *Angewandte Chemie International Edition* 44 (2005) 797.
- [39] S.M. Yuan, J.X. Li, L.T. Yang, L.W. Su, L. Liu, Z. Zhou, *Applied Materials & Interfaces* 3 (2011) 705.
- [40] C. Burda, X.B. Chen, R. Narayanan, M.A. El-Sayed, *Chemical Reviews* 105 (2005) 1025.
- [41] H. Liu, G.X. Wang, J. Liu, S.Z. Qiao, H. Ahn, *Journal of Materials Chemistry* 21 (2011) 3046.

- [42] T. Kavitha, H. Yuvaraj, *Journal of Materials Chemistry* 21 (2011) 15686.
- [43] N. Yan, L. Hu, Y. Li, Y. Wang, H. Zhong, X.Y. Hu, X.K. Kong, Q.W. Chen, *The Journal of Physical Chemistry C* 116 (2012) 7227.
- [44] X.W. Lou, D. Deng, J.Y. Lee, J. Feng, L.A. Archer, *Advanced Materials* 18 (2008) 4397.
- [45] Y. Liu, X.G. Zhang, *Electrochimica Acta* 54 (2009) 4180.
- [46] S. Grugeon, S. Laruelle, R. Herrera-Urbina, L. Dupont, P. Poizot, J.M. Tarascon, *Journal of the Electrochemical Society* 148 (2001) A285.
- [47] J.X. Zhu, Y.K. Sharma, Z.Y. Zeng, X.J. Zhang, M. Srinivasan, S. Mhaisalkar, H. Zhang, H.H. Hng, Q.Y. Yan, *The Journal of Physical Chemistry C* 115 (2011) 8400.
- [48] X.W. Lou, D. Deng, J.Y. Lee, L.A. Archer, *Journal of Materials Chemistry* 18 (2008) 4397.
- [49] S.A. Needham, G.X. Wang, H.K. Liu, *Journal of Power Sources* 159 (2006) 254.
- [50] X.H. Huang, J.P. Tu, C.Q. Zhang, J.Y. Xiang, *Electrochemistry Communications* 9 (2007) 1180.
- [51] L. Liu, Y. Li, S.M. Yuan, M. Ge, M.M. Ren, C.S. Sun, Z. Zhou, *Journal of Physical Chemistry C* 114 (2010) 251.
- [52] M.M. Rahman, S.L. Chou, C. Zhong, J.Z. Wang, D. Wexler, H.K. Liu, *Solid State Ionics* 180 (2010) 1646.
- [53] B. Varghese, M.V. Reddy, Z. Yanwu, C.S. Lit, T.C. Hoong, G.V. Subba Rao, B.V.R. Chowdari, A.T.S. Wee, C.T. Lim, C.H. Sow, *Chemistry of Materials* 20 (2008) 3360.
- [54] A. Débart, L. Dupont, P. Poizot, J.B. Leriche, J.M. Tarascon, *Journal of the Electrochemical Society* 148 (2001) A1266.
- [55] S.A. Needham, G.X. Wang, H.K. Liu, *Journal of Power Sources* 159 (2006) 254.